832c

OPTICAL DENSITY FORMATION IN TRACK-ETCH RADIOGRAPHY

by

WOLFGANG JOACHIM HARTMANN, B.Sc.

PART A: McMASTER (OFF-CAMPUS) PROJECT*

A

Report Submitted to the School of Graduate Studies

in Partial Fulfilment of the Requirements

for the Degree

Master of Engineering

November 1975

*One of two project reports: The other part is designated PART B: ON-CAMPUS PROJECT

MASTER OF ENGINEERING (1975)
Department of Engineering Physics

McMASTER UNIVERSITY
Hamilton, Ontario

TITLE: Optical Density Formation in Track-Etch Radiography

AUTHOR: Wolfgang Joachim Hartmann, B.Sc.(Calgary, Alberta)

SUPERVISOR: Dr. A.A. Harms

NUMBER OF PAGES: viii, 58

ABSTRACT

Track-etch imaging is investigated as a recording method for neutron radiographic purposes. A theoretical model is formulated and evaluated together with experimental data which is analyzed in an attempt to explore the possibility of maximizing optical contrast. A central converter system with Lithium-6 as the converter and cellulose-nitrate as the recorders is used. It is found that the maximum contrast is achieved by using a clear cellulose-nitrate recorder at least 10 μm thick and a Lithium-6 converter of approximately 140 μm thickness.

ACKNOWLEDGEMENTS

The author wishes to thank Dr. A.A. Harms, Department of Engineering Physics, for his guidance in the preparation of this project. Discussions with Dr. R.H. Stinson, University of Guelph, are greatly appreciated. The author also wishes to thank Mr. F. Smith, Mr. F. Pearson, Mr. E. Hartmann, and Mr.A. Singh for their technical assistance.

LIST OF FIGURES

PAGE

Fig. 1: Schematic representation of central converter arrangements 4

Fig. 2: Illustration showing arrangement of converter, recorder, and cassette 5

Fig. 3: Schematic illustration showing neutron interactions in the converter and track formation in the recorder for the front recorder arrangement 10

Fig. 4: Track formation representations as described in Section 3.2 14

Fig. 5: (a) Track etch formation domains for a converter thickness of 150 μm. 30

(b) Track etch formation domains for a converter thickness of 40 μm. 31

Fig. 6: Dependence of optical density on Lithium-6 converter thickness for the front recorder system 40

Fig. 7: Dependence of optical density on Lithium-6 converter thickness for the back recorder system 41

Fig. 8: Comparison between the one-dimensional optical density model and the three-dimensional optical density model for the central converter system 42

Fig. 9: Electron micrographs of etch-pit profiles at 70° of incidence 47

Fig. 10: Transmission photo-micrograph of CN-recorder 48

Fig. 11: Reflection photo-micrograph of CN-recorder 49

Fig. 12: Experimental transmission data of optical density versus Lithium-6 converter thickness for the Roman numeral set, obtained by using red (6600 A) light 50

Fig. 13: Experimental transmission data of optical density versus Lithium-6 converter thickness for the Arabic numeral set, obtained by using red (6600 A) light 51

LIST OF TABLES

PAGE

Table I: Track-etch parameters used in the analysis 35

Table II: Comparison between the integral of Case I front and back recorder triton optical density, as a function of the lithium converter thickness as obtained from theory 36

Table III: Comparison between the integral of Case II front and back recorder triton optical densities, as a function of the lithium converter thickness as obtained from theory 37

Table IV: Comparison between the integral of Case II front and back recorder alpha-particle optical densities, as a function of the lithium converter thickness as obtained by theory 38

Table V: Alpha-particle and triton total optical density contributions, for front-, back-, and central converter systems as a function of lithium converter thickness 39

Table VI: Organization of the experimental data 46

TABLE OF CONTENTS

		PAGE
ABSTRACT		iii
ACKNOWLEDGEMENTS		iv
LIST OF FIGURES		v
LIST OF TABLES		vi
CHAPTER 1:	INTRODUCTION	1
CHAPTER 2:	SYSTEM DESCRIPTION	3
CHAPTER 3:	SYSTEM THEORY	
	3.1 Introduction	7
	3.2 Physical Modelling and Mathematical Derivation	8
	3.3 Analysis of the Theoretical Derivation	20
	3.4 Application of the Theory to the Lithium-6 Converter, Triton and Alpha-Particle Recording Central Converter System	29
CHAPTER 4:	EXPERIMENTAL DATA ANALYSIS AND RESULTS	
	4.1 Method Description	43
	4.2 Discussion of the Measurement Technique	44
	4.3 Presentation of the Data	44
CHAPTER 5:	DISCUSSION OF THE RESULTS	
	5.1 Theoretical-Experimental Curve Fitting	52
	5.2 Cellulose Nitrate Film Colouration	52
	5.3 Saturation Effects	54
	5.4 Cellulose Nitrate Film Thickness	55

PAGE

CHAPTER 6: CONCLUSION 56

REFERENCES 57

CHAPTER 1

INTRODUCTION

Neutron radiography has become an important method for the non-destructive examination of material products. The increasing use of neutron radiography has been aided by the rapid development of nuclear reactors which ensure the necessary neutron source and by the need of a supplement for the already well established x-ray and gamma-ray techniques for non-destructive material testing.

Track-etch imaging has become a widely used method for charged particle-track registration in a number of fields such as nuclear physics, astrophysics, geophysics, and biophysics.[1-5] Since only charged particles are recorded, neutrons cannot produce tracks directly and a converter has to be located adjacent to the sensitive film. Usually Boron-10 or Lithium-6 are used which produce alpha-particles and tritons when reacting with neutrons.[6] The major advantages of the track-etch method are:

(i) no interfering electromagnetic radiation can be recorded;

(ii) track-etch image processing and viewing can be done immediately after exposure;

(iii) in a mixed radiation field, the lack of sensitivity to x and gamma radiation, and beta particles presents an advantage when only heavy charged particles are to be recorded;[5]

(iv) extremely high spatial resolution can be obtained.[7]

The major disadvantage is that the image often possesses a low contrast.

This experimental and theoretical study was undertaken in an attempt to improve the contrast and clarify previous theoretical treatments[6] of the same problem. Special consideration was given to the type of recording film to be used and both exposure times and converter thicknesses were varied.

CHAPTER 2

SYSTEM DESCRIPTION

The track-etch system studied was the central converter arrangement as illustrated in Fig. 1. This arrangement was used since it was found to be the most efficient.[8] Pure Lithium-6, in its metallic form was used as a converter. Strips of lithium were obtained by cold rolling. Their dimensions were about 2 mm in width and varied from 30 μm to 200 μm in thickness. These lithium strips were sandwiched between two cellulose-nitrate recording films. The central converter system was then enclosed between two aluminum plates which were fastened tightly together to ensure close contact. This arrangement is shown in Fig. 2. The sensitive film used was Kodak experimental film LR 115, which consisted of an 8 μm layer of cellulose-nitrate dyed red on a 100 μm backing of clear polyester base. The etching was done in a sodium hydroxide solution in which the concentration was 10% by weight at a temperature of 60°C. The developing time was about 60 minutes during which time about 2.6 μm of the cellulose-nitrate layer was removed at undamaged film regions.[7] The damaged regions, or the particle tracks, which are caused by ionization damage as the particles are slowed down, etch out fourteen times faster and thus produce visible etch-craters with diameters between 1 μm and 7 μm.[1,7] A submerged neutron beam facility installed in the pool of the McMaster

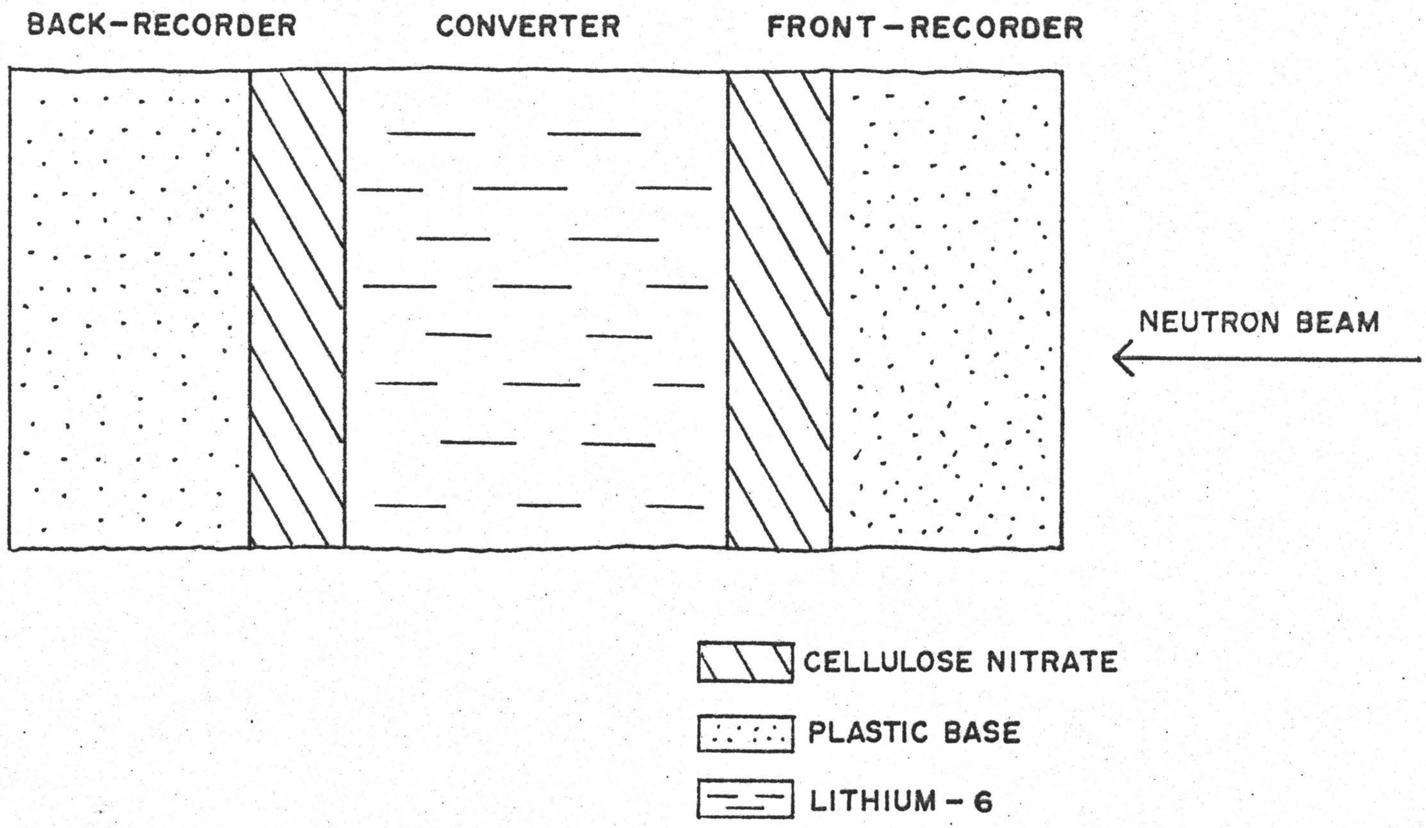

Fig. 1: Schematic representation of central converter arrangements

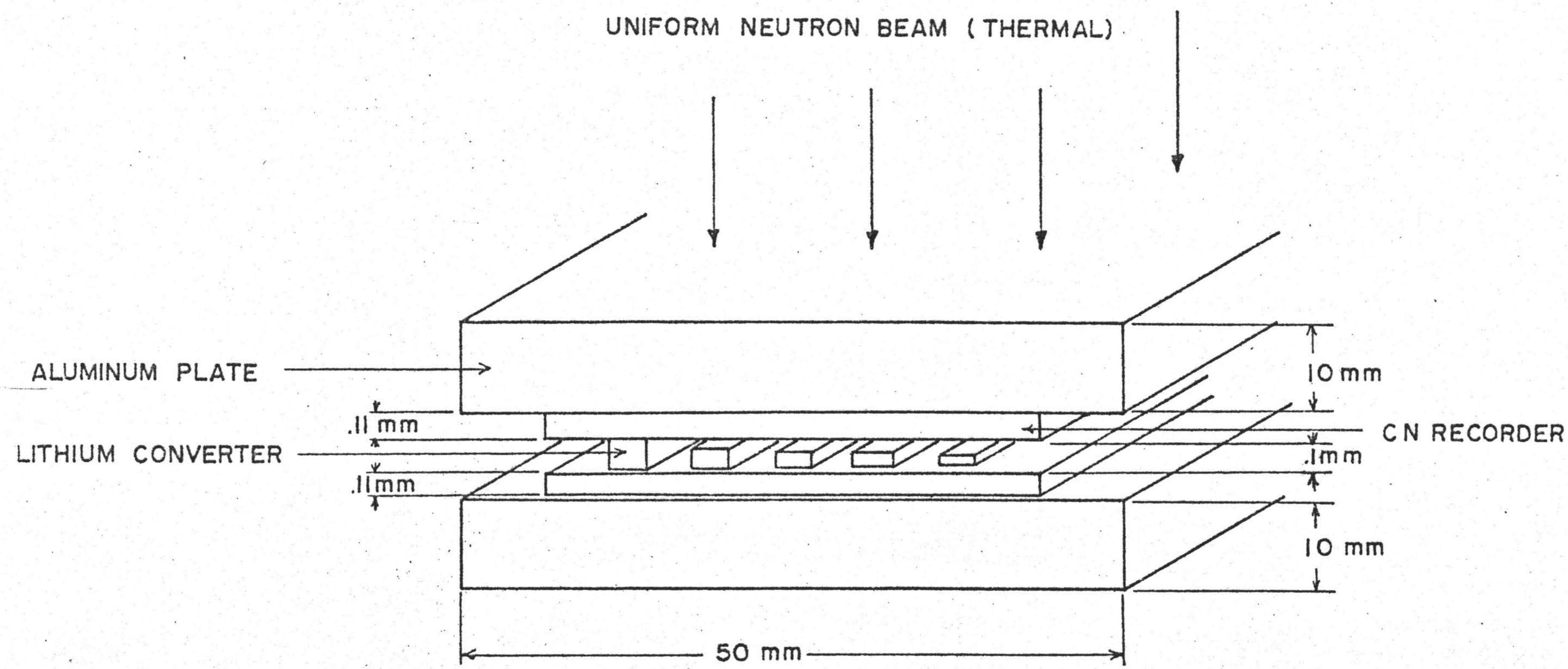

Fig. 2: Illustration showing arrangement of converter, recorder, and cassette

University Nuclear Reactor (5MWt) was used as the neutron source. The neutron flux at the image plane was of the order of 3×10^7 n/cm^{-2}sec^{-1}.

CHAPTER 3

SYSTEMS THEORY

3.1 Introduction

It is not difficult to calculate the volume of etched-away track damage produced by charged particles, such as an alpha-particle or triton, in cellulose-nitrate recording film. A model can be constructed for the optical density of a central converter recording arrangement if it is assumed that the etched-out track volume is proportional to the optical density. Experimental evidence shows that two effects - further discussed under experimental results - have to be considered when track volume and optical density relationships are determined.

1. Each track-volume acts as a scattering centre, produced by the rough track-walls. Considering transmission optical densities, it is therefore, possible to conclude that the optical density is directly proportional to the track-volume.
2. For coloured recording film, any volume etched away will increase the light transmission, since potential absorbtive medium is removed. This means that the optical density is inversely proportional to the track volume.

Thus we have two effects competing with each other and any actual recording will exhibit a combination of both cases. Under certain circumstances, the second case can be suppressed so that its effect can be reduced. This is done by ensuring that tracks do not etch right through the recording layer thus preventing the recorder from saturating. In addition, the recording material should be clear and colourless. Under these conditions, the theory is very useful and practical. The second effect will only be visible as a higher order perturbation and will become important only in recorder saturation cases when scattering centres overlap considerably and thus forms a uniform background density which is basically independent of the converter thickness. Obviously any colouration of the recording material will amplify the second effect producing an optical density which, apart from an initial density build up, will be a function of the number of tracks penetrating the recorder completely.

In the following derivation, the central converter system is split into two cases:

1. the front recorder system,
2. the back recorder system.

Each system is treated separately in the above order.

3.2 Physical Modelling and Mathematical Derivation

To find the track-volume as recorded by a recording film, one first has to obtain an expression for the charged particle flux contribution from the converter as a function of the location of the flux producing element in the converter. At this stage we assume a thermal, uniform neutron beam which ensures a uniform charged particle flux in all directions from the particle's origin. The particle flux as a function of its location of origin in the converter is thus given by F(r), where:(6)

$$F(r) \propto \Sigma_\alpha \phi(r) \Delta V \quad , \tag{3.1a}$$

or

$$F(r) = C\Sigma_\alpha \phi(r) \Delta V \quad . \tag{3.1b}$$

Here C is a constant of proportionality, Σ_α is the macroscopic absorption cross-section, ΔV is the volume element at location (r) under consideration and $\phi(r)$ is the incident neutron flux, given by

$$\phi(r) = \phi_o \exp[- \Sigma_\alpha r\cos\theta] \quad , \tag{3.2}$$

where $[r\cos\theta]$ is the distance from the converter surface to the volume element P_V as illustrated in Fig. 3.

The volume element at P_V is given by Eq. (3.3) using spherical coordinates:

$$\Delta V = \Delta r \times r\Delta\theta \times r\sin\theta\Delta\phi \quad . \tag{3.3}$$

For the analysis, consider all charged particles passing through area "A" at r = 0, Fig. 3, which is part of the converter-recorder interface plane. These particles will form tracks of length $R^*_{r,\theta}$ in the recorder. Let ξ be the cross sectional area of the track, then the volume of the track, V_{TR}, is given by

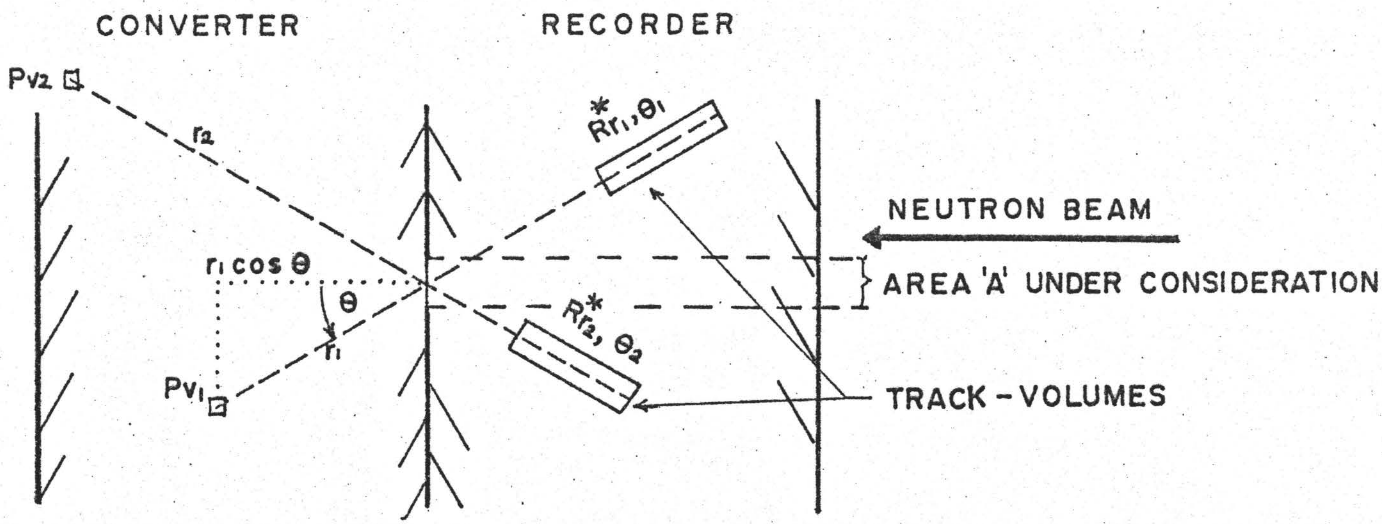

Fig. 3: Schematic illustration showing neutron interactions in the converter and track formation in the recorder for the front recorder arrangement

$$V_{TR} = \xi R^{*}_{r,\theta} \quad . \tag{3.4}$$

To obtain the total contribution of track-volumes caused by particles passing through "A", the entire converter volume has to be considered as a potential contributor. Expressed in integral form, the optical density, D^{*}, is thus given by combining Eq. (3.1) to Eq. (3.4):

$$D^{*} = \int_{r}\int_{\theta}\int_{\phi} CC_{1}(r,\theta)(R^{*}_{r,\theta}\xi)\Sigma_{\alpha}\phi_{o}\exp[-\Sigma_{\alpha}r\cos\theta]r^{2}\sin\theta dr d\theta d\phi \quad . \tag{3.5}$$

The weighting function $C_{1}(r,\theta)$ is necessary since volume elements with different r and θ values, defining locations of P_{V}, contribute to a flux of different magnitude. This is due to the source-recorder distance, r, which introduces the inverse square law of flux intensities. There is also an angular dependence since sources at P_{V} "see" the area "A" at different angles of incidence. From these considerations, the weighting function may be written as

$$C_{1}(r,\theta) = \frac{1}{r^{2}}\cos\theta \quad . \tag{3.6}$$

Combining Eq. (3.5) and Eq. (3.6) we obtain

$$D^{*} = \int_{r}\int_{\theta}\int_{\phi} R^{*}_{r,\theta}\xi C\phi_{o}\Sigma_{\alpha}\exp[-\Sigma_{\alpha}r\cos\theta]\sin\theta\cos\theta dr d\theta d\phi \quad , \tag{3.7}$$

which after integrating over ϕ from 0 to 2π gives

$$D^{*} = \int_r \int_\theta 2\pi C R^{*}_{r,\theta} \xi \Sigma_\alpha \phi_o \exp[-\Sigma_\alpha r\cos\theta]\sin\theta\cos\theta\, dr\, d\theta \quad . \tag{3.8}$$

At this point all constants, which can be taken out of the integral, are set equal to one. This can be done since the optical density, D, can be normalized to fit actual experimental data. All constants are thus taken care of. The parameter ξ is assumed to be a constant. Therefore by letting

$$D = \frac{D^{*}}{C\xi\Sigma_\alpha \phi_o 2\pi}$$

we obtain

$$D = \int_r \int_\theta R^{*}_{r,\theta} \exp[-\Sigma_\alpha r\cos\theta]\sin\theta\cos\theta\, dr\, d\theta \quad . \tag{3.10}$$

Before any further integration can be done, an exact expression for $R^{*}_{r,\theta}$ has to be determined. Two cases have to be considered:[11]

Case I: the etchable track is completely imbedded in the recorder, and

Case II: the particle has already attained the threshold energy in the converter, thus making it possible for the etchable track to start right at the converter-recorder interface.

Figure 4 illustrates both cases.

First Case I is considered and is broken up into two subcases:

Case I(a): the track is not etched out completely due to a lack of etch-time, and

Case I(b): the track is completely etched out and etching continues after the track etch is completed, Fig. 5.

Again Case I(a) is considered first.

Let the etch velocity of the damaged track region be V_D and assume V_D to be constant. Also let the normal etch velocity of the undamaged region be V_N. Then the effective track length is defined by:

$$R^{*1a}_{r,\theta} = \text{track length etched - normal background etching during the same time as previous term} \quad , \qquad (3.11a)$$

that is

$$R^{*1a}_{r,\theta} = V_D t_3 - \frac{r_3}{\cos\theta} \quad , \qquad (3.11b)$$

where t_3 is the etch time left at the beginning of the track-etch and the parameter r_3, Fig. 4, is given by:

$$r_3 = t_3 V_N \quad . \qquad (3.12)$$

By combining Eq. (3.11b) and Eq. (3.12) we obtain

$$R^{*1a}_{r,\theta} = Vr_3 - \frac{1}{\cos\theta} r_3 \quad , \qquad (3.13)$$

where the substitution

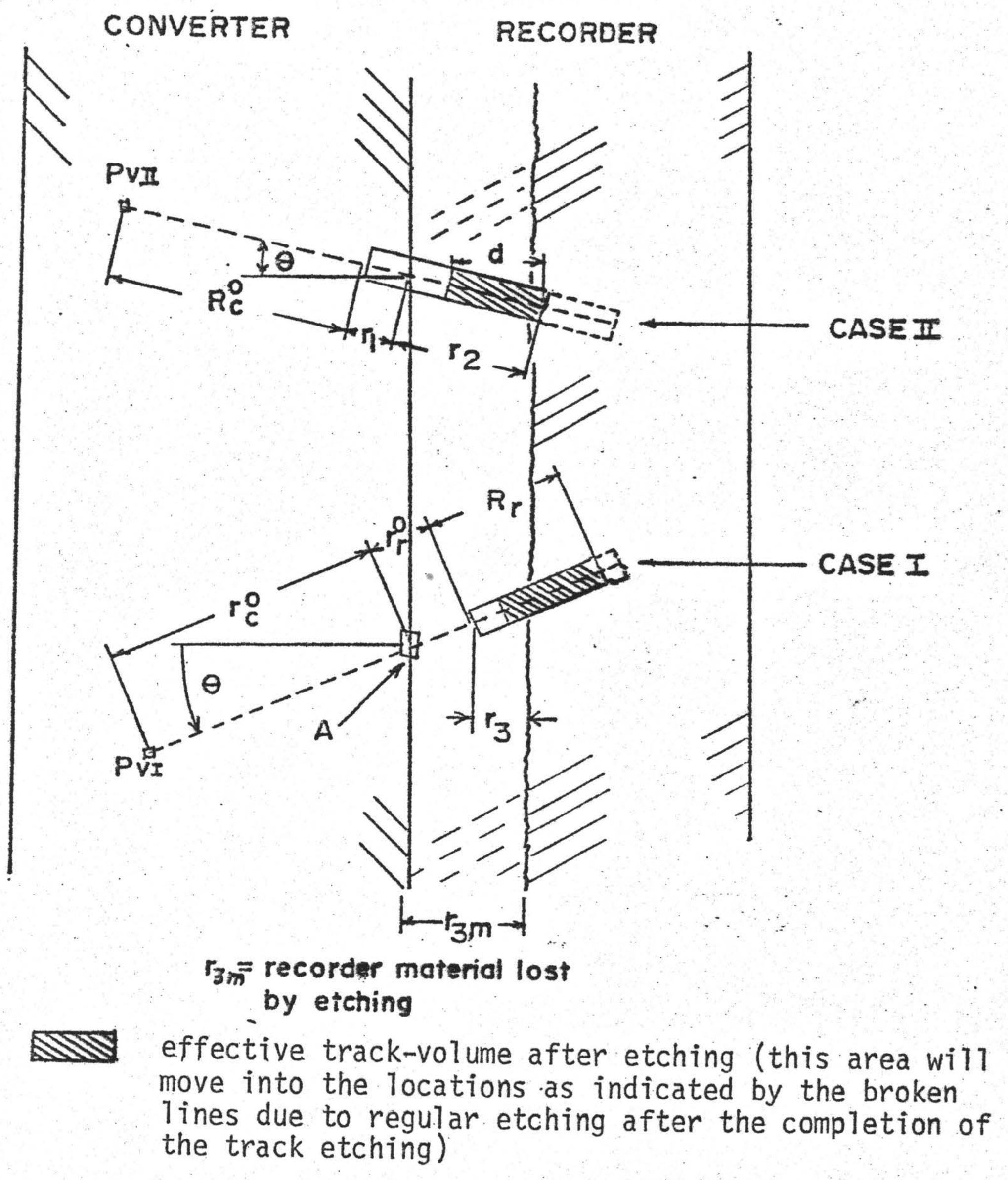

Fig. 4: Track formation representations as described in Section 3.2

$$V = \frac{V_D}{V_N} \quad , \tag{3.14}$$

has been made.

Rearranging Eq. (3.13) we obtain:

$$R^{*1a}_{r,\theta} = Vr_3[1 - \frac{1}{V\cos\theta}] \quad . \tag{3.15}$$

Now Case I(b) is considered. Equation (3.11a) is still correct, and is expressed by:

$$R^{*1b}_{r,\theta} = R_r - t_2 \frac{V_N}{\cos\theta} \quad . \tag{3.16}$$

Here R_r is defined as the track length of the charged particle in the recorder and t_2, the time needed for the track length, R_r, to be etched out, is given by:

$$t_2 = \frac{R_r}{V_D} \quad . \tag{3.17}$$

Combining Eq. (3.16) and Eq. (3.17) we obtain

$$R^{*1b}_{r,\theta} = R_r - \frac{R_r V_N}{V_D \cos\theta}$$

or

$$R^{*1b}_{r,\theta} = R_r[1 - \frac{1}{V\cos\theta}] \quad . \tag{3.18}$$

Clearly, Case I(a) is applicable when

$$Vr_3 < R_r \quad ,$$

and hence Cases I(a) and I(b) can therefore be written as

$$R^{*1}_{r,\theta} = K^{*1}_{r,\theta}[1 - \frac{1}{V\cos\theta}] \quad , \tag{3.19}$$

where

$$K^{*1}_{r,\theta} = Vr_3, \quad \text{if } Vr_3 < R_r \quad ,$$

and

$$K^{*1}_{r,\theta} = R_r \quad , \quad \text{if } Vr_3 \geq R_r \quad .$$

Since negative track lengths are not defined, we set

$$R^{*1}_{r,\theta} = 0 \quad ,$$

whenever Eq. (3.19) defines a negative effective track length.

The only undefined variable is r_3, Fig. 4, which is now evaluated. Etchable tracks are only obtained when the particle has reached energies below the threshold energy. The unetchable track sections in the converter, r°_c, and in the recorder, r°_r, (see Fig. 4) are related by

$$\frac{r^\circ_c}{R^\circ_c} + \frac{r^\circ_r}{R^\circ_r} = 1 \quad , \tag{3.20}$$

where R°_c = effective track length of the particle in the converter, while the particle slows down from its initial energy to its threshold energy, and

R_r° = effective track length of the particle in the recorder, while the particle slows down from its initial energy to its threshold energy.

Solving Eq. (3.20) for r_r° we obtain:

$$r_r^\circ = R_r^\circ[1 - \frac{r_c^\circ}{R_c^\circ}] \quad . \tag{3.21}$$

Using Fig. 4, the following equation is obtained:

$$\frac{r_{3m} - r_3}{r_r^\circ} = \cos\theta \quad , \tag{3.22}$$

or

$$r_{3m} - r_r^\circ\cos\theta = r_3 \quad . \tag{3.23}$$

Making use of Eq. (3.23) and noting that $r_c^\circ = r$, Eq. (3.21) can be rewritten as:

$$r_3 = [\frac{r}{R_c^\circ} - 1]R_r^\circ\cos\theta + r_{3m} \quad . \tag{3.24}$$

We now consider Case II. The relationship between r_1 and r_2, the "etchable" track lengths in converter and recorder, as defined by Fig. 4, is given by

$$\frac{r_1}{R_c} + \frac{r_2}{R_r} = 1 \quad . \tag{3.25}$$

Here R_c = effective track length of the particle below threshold energy in the converter,

and

R_r = effective etchable track length of the particle in the recorder.

Solving Eq. (3.25) for r_2, we obtain

$$r_2 = R_r[1 - \frac{r_1}{R_c}] \quad , \tag{3.26}$$

where r_1 is given by

$$r_1 = r - R_c^\circ \quad . \tag{3.27}$$

Combining Eq. (3.26) and Eq. (3.27) we obtain

$$r_2 = R_r[1 - \frac{(r - R_c^\circ)}{R_c}] \, . \tag{3.28}$$

Similar to Case I, the etched track length, $R^{*2}_{r,\theta}$ is given by

$$R^{*2}_{r,\theta} = r_2 - t_3 \frac{V_N}{\cos\theta} \quad , \tag{3.29}$$

where

$$t_3 = \frac{r_2}{V_D} \quad . \tag{3.30}$$

Using Eq. (3.30) and letting $r_2 = K^{*2}_r$, we can write Eq. (3.29) as

$$R^{*2}_{r,\theta} = r_2[1 - \frac{1}{V\cos\theta}] \quad , \tag{3.31}$$

or

$$R^{*2}_{r,\theta} = K^{*2}_{r}[1 - \frac{1}{V\cos\theta}] \quad . \tag{3.32}$$

Here if $K^{*2}_{r} < 0$ or $[1 - \frac{1}{V\cos\theta}] < 0$, then $R^{*2}_{r,\theta}$ is set equal to zero.

At this point, Eq. (3.10) can be reconsidered. The optical density in the front recorder case, as illustrated by Fig. 3, is now given by

$$D = \int_r\int_\theta K^{*1,2}_{r,\theta}[1 - \frac{1}{V\cos\theta}]\exp(-\Sigma_\alpha r\cos\theta)\sin\theta\cos\theta drd\theta \quad , \tag{3.33}$$

where

$$K^{*1,2}_{r,\theta} \geqslant 0 \qquad \text{or zero} \quad , \tag{3.34}$$

and

$$[1 - \frac{1}{V\cos\theta}] \geqslant 0 \qquad \text{or zero} \quad . \tag{3.35}$$

When $r - R^\circ_c > 0$, then K^{*2}_{r} is used and when $r - R^\circ_c < 0$, then $K^{*1}_{r,\theta}$ is used. These parameters are given by

$$K^{*1}_{r,\theta} = Vr_3 \qquad \text{if } Vr_3 < R_r \quad , \tag{3.19}$$

$$r_3 = [\frac{r}{R^\circ_c} - 1]R^\circ_r\cos\theta + r_{3m} \quad , \tag{3.24}$$

$$K^{*1}_{r} = R_r \qquad \text{if } Vr_3 \geqslant R_r \quad , \tag{3.19}$$

and

$$K_r^{*2} = R_r[1 - \frac{(r - R_c^\circ)}{R_c}] \quad . \tag{3.32}$$

In Fig. 5, Case I and Case II leading to density distributions D(I) and D(II) are illustrated (A Li-converter-T-producing system is considered).

3.3 Analysis of the Theoretical Derivation

To solve the integral (3.33), let us first consider Case II, since it is easily solved. Case II is defined as having an r-range from $r = R_c^\circ$ to $r = R_c^\circ + R_c$. First the integral (3.33) is written as

$$D_{II} = \int_r K_r^{*2} \int_\theta [1 - \frac{1}{V\cos\theta}] \exp(-\Sigma_\alpha r\cos\theta)\sin\theta\cos\theta d\theta dr \quad . \tag{3.36}$$

The angular integral can be rearranged to give

$$I_\theta = \int_{\theta_\ell}^{\theta_u} \exp(-\Sigma_\alpha r\cos\theta)\sin\theta\cos\theta d\theta -$$

$$\int_{\theta_\ell}^{\theta_u} \frac{1}{V} \exp[-\Sigma_\alpha r\cos\theta)\sin\theta d\theta \quad . \tag{3.37}$$

Letting

$$\Sigma_\alpha r = -C_2 \quad , \tag{3.38}$$

and making the substitution

$$u = \cos\theta \quad , \frac{du}{d\theta} = -\sin\theta \quad , \tag{3.39}$$

we obtain

$$I_\theta = \int_{U_\ell}^{U_u} - \exp(C_2U)udu + \int_{U_\ell}^{U_u} \frac{1}{V}\exp(C_2U)du \quad , \tag{3.40}$$

which is easily integrated to give

$$I_\theta = -\frac{\exp(C_2U_u)}{C_2^2}[C_2U_u - 1] + \frac{\exp(C_2U_\ell)}{C_2^2}[C_2U_\ell - 1]$$

$$+ \frac{1}{VC_2}\exp(C_2U_u) - \frac{1}{VC_2}\exp(C_2U_\ell) \quad . \tag{3.41}$$

Since $\theta_u = \text{arc}\cos\frac{1}{V}$ and therefore $U_u = \frac{1}{V}$, the integral equation can be written as

$$I_\theta = \frac{\exp(C_2\frac{1}{V})}{C_2^2} + \frac{\exp(C_2U_\ell)}{C_2}(U_\ell - \frac{1}{C_2} - \frac{1}{V}) \quad . \tag{3.42}$$

Using Eq. (3.42), we reformulate Eq. (3.36) to give

$$D_{II} = \int_r K_r^{*2}[\frac{\exp(C_2\frac{1}{V})}{C_2^2} + \frac{\exp(C_2U_\ell)}{C_2}(U_\ell - \frac{1}{C_2} - \frac{1}{V})]dr \quad . \tag{3.43}$$

The lower angular limit, θ_ℓ, depends on the value of r, Fig. 5, used in the integration. If $r \leq L$, where L is the converter thickness, then

$$\theta_\ell = 0 \quad \text{or } U_\ell = 1$$

If $r > L$ then

$$\theta_\ell = \arc\cos\frac{L}{r} \quad \text{or } U_\ell = \frac{L}{r}$$

where r also has to be within the limits of Case II. Equation (3.43), must therefore be split into two integrals, Fig. 5, which can be expressed as

$$D_{II}\int_L^{R_c^\circ+R_c} K_r^{*2}\left[\frac{\exp(C_2\frac{1}{V})}{C_2^2}+\frac{\exp(C_2\frac{L}{r})}{C_2}\left(\frac{L}{r}-\frac{1}{C_2}-\frac{1}{V}\right)\right]dr +$$

$$\int_{R_c^\circ}^{L} K_r^{*2}\left[\frac{\exp(C_2\frac{1}{V})}{C_2^2}+\frac{\exp C_2}{C_2}\left(1-\frac{1}{C_2}-\frac{1}{V}\right)\right]dr \quad . \tag{3.44}$$

The second integral is zero when $L < R_c^\circ$ or the limit L is replaced by R_c°. This case is illustrated in Fig. 5b. Equation (3.44) can be written in the form

$$D_{II} = D_{II_1} + D_{II_2}$$

such that

$$D_{II_1} = \int_{r_{\ell_1}}^{r_{u_1}} R_r[1 - \frac{(r - R_c^\circ)}{R_c}][\frac{\exp(- \Sigma_\alpha \frac{r}{V})}{\Sigma_\alpha^2 r^2}$$

$$+ \frac{\exp(- \Sigma_\alpha L)}{- \Sigma_\alpha r} (\frac{L}{r} + \frac{1}{\Sigma_\alpha r} - \frac{1}{V})]dr \quad . \tag{3.45}$$

After expanding and collecting terms, we obtain

$$D_{II_1} = \int_{r_{\ell_1}}^{r_{u_1}} \exp(ar) \frac{1}{r^2} S_1 + \exp(ar) \frac{1}{r} S_2$$

$$+ \frac{1}{r^2} S_3 + \frac{1}{r} S_4 + S_5 dr \quad , \tag{3.46}$$

where

$$a = - \frac{\Sigma_\alpha}{V} \quad ,$$

$$S_1 = \frac{R_r}{\Sigma_\alpha^2} (1 - \frac{R_c^\circ}{R_c}) \quad ,$$

$$S_2 = - \frac{R_r}{R_c \Sigma_\alpha^2} \quad ,$$

$$S_3 = [\exp(- \Sigma_\alpha L)] \frac{R_r}{\Sigma_\alpha} (- L - \frac{1}{\Sigma_\alpha} - \frac{R_c^\circ L}{R_c} - \frac{R_c^\circ}{R_c \Sigma_\alpha}) \quad ,$$

$$S_4 = [\exp(- \Sigma_\alpha L)] \frac{R_r}{\Sigma_\alpha} (\frac{1}{V} + \frac{L}{R_c} + \frac{1}{R_c \Sigma_\alpha} + \frac{R_c^\circ}{R_c V}) \quad ,$$

$$S_5 = - \frac{R_r}{R_c V \Sigma_\alpha} [\exp(- \Sigma_\alpha L)] \quad .$$

Integration of Eq. (3.45) is now possible by using Tables.[9] We note that in the case of $|ar| < 1$, we can omit higher order terms. The optical density contribution can therefore be written

$$D_{II_1} = S_1[- \exp(ar_{u1}) \frac{1}{r_{u1}} + a(\ln r_{u1} + ar_{u1} + \frac{a^2 r_{u1}^2}{4} \ldots)$$

$$+ \exp(ar_{\ell 1}) \frac{1}{r\ell_1} - a(\ln r_{\ell 1} + ar_{\ell 1} + \frac{a^2 r_{\ell 1}^2}{4} \ldots)]$$

$$+ S_2[(\ln r_{u1} + ar_{u1} + \frac{a^2 r_{u1}^2}{4} \ldots) - (\ln r_{\ell 1} + ar_{\ell 1} + \frac{a^2 r_{\ell 1}^2}{4} \ldots)]$$

$$+ S_3[\frac{-1}{r_{u1}} + \frac{1}{r_{\ell 1}}] + S_4[\ln r_{u1} - \ln r_{\ell 1}] + S_5[r_{u1} - r_{\ell 1}] \quad , \qquad (3.47)$$

where the limits r_{u1} (upper (1)) and $r_{\ell 1}$ (lower (1)) are defined by Eq. (3.44).

Now the second integral, D_{II_2}, defined by Eq. (3.44) is solved. Using Eq. (3.32) and Eq. (3.38), the second integral may be written as

$$D_{II_2} = \int_{r_{\ell 2}}^{r_{u2}} R_r[1 - \frac{(r - R_c^\circ)}{R_c}][\exp(- \frac{\Sigma_\alpha r}{V}) \frac{1}{\Sigma_\alpha^2 r^2}$$

$$+ \exp(- \Sigma_\alpha r) \frac{1}{- \Sigma_\alpha r} (1 + \frac{1}{\Sigma_\alpha r} - \frac{1}{V})]dr \quad . \qquad (3.48)$$

After expanding and collecting terms, we obtain:

$$D_{II_2} = \int_{r_{\ell 2}}^{r_{u2}} \exp(ar)\,\frac{1}{r^2}\,S_6 + \exp(ar)\,\frac{1}{r}\,S_7$$

$$+ \exp(aVr)\,\frac{1}{r^2}\,S_8 + \exp(aVr)\,\frac{1}{r}\,S_9$$

$$+ \exp(aVr)\,S_{10}dr \quad , \tag{3.49}$$

where

$$a = -\frac{\Sigma_\alpha}{V} \quad ,$$

$$S_6 = S_1 \quad ,$$

$$S_7 = S_2 \quad ,$$

$$S_8 = -\,S_1 \quad ,$$

$$S_9 = \frac{R_r}{\Sigma_\alpha}\left(-\,1 + \frac{1}{V} + \frac{1}{R_c\Sigma_\alpha} - \frac{R_c^\circ}{R_c} + \frac{R_c^\circ}{R_cV}\right) \quad ,$$

$$S_{10} = \frac{R_r}{\Sigma_\alpha R_c}\left(1 - \frac{1}{V}\right) \quad .$$

As before, we integrate and obtain

$$D_{II_2} = S_6[-\exp(ar_{u2})\frac{1}{r_{u2}} + a(\ln r_{u2} + ar_{u2} + \frac{a^2r_{u2}^2}{4}\ldots)$$

$$+ \exp(ar_{\ell 2})\frac{1}{r_{\ell 2}} - a(\ln r_{\ell 2} + ar_{\ell 2} + (\frac{ar_{\ell 2}}{2})^2\ldots)]$$

$$+ S_7[(\ln r_{u2} + ar_{u2} + (\frac{ar_{u2}}{2})^2\ldots) - (\ln r_{\ell 2} + ar_{\ell 2} + (\frac{ar_{\ell 2}}{2})\ldots)]$$

$$+ S_8[-\exp(aVr_{u2})\frac{1}{r_{u2}} + aV(\ln r_{u2} + aVr_{u2} + (\frac{aVr_{u2}}{2})^2$$

$$+ \frac{(aVr_{u2})^3}{18} + \frac{(aVr_{u2})^4}{96}\ldots) + \exp(aVr_{\ell 2})\frac{1}{r_{\ell 2}}$$

$$- aV(\ln r_{\ell 2} + aVr_{\ell 2} + \frac{(aVr_{\ell 2})^2}{4} + \frac{(aVr_{\ell 2})^3}{18} + \frac{(aVr_{\ell 2})^4}{96}\ldots)]$$

$$+ S_9[(\ln r_{u2} + aVr_{u2} + \frac{(aVr_{u2})^2}{4} + \frac{(aVr_{u2})^3}{18} + \frac{(aVr_{u2})^4}{96} + \ldots)$$

$$- (\ln r_{\ell 2} + aVr_{\ell 2} + \frac{(aVr_{\ell 2})^2}{4} + \frac{(aVr_{\ell 2})^3}{18} + \frac{(aVr_{\ell 2})^4}{96}\ldots)]$$

$$+ S_{10}[\frac{1}{aV}\exp(aVr_{u2}) - \frac{1}{aV}\exp(aVr_{\ell 2})] \quad . \tag{3.50}$$

Again the limits r_{u2} (upper II)) and $r_{\ell 2}$ (lower II)) are defined by Eq. (3.44). In summary, the complete solution for Case II is given by

$$D_{II} = D_{II_1} + D_{II_2} \quad , \tag{3.51}$$

where D_{II_1} is given by Eq. (3.47) and D_{II_2} is given by Eq. (3.50).

Now Case I is reconsidered. Case I is defined as having a range from $r = 0$ to $r = R_c^\circ$ as illustrated by Fig. 5. The number of different conditions for limits and constants make the integral (3.33) difficult to solve. The integral has to be changed into the form of a summation and then only a numerical solution is possible. The summation obtained is

$$D_I = \sum_{\Delta r\ r=o}^{r=L} \sum_{\Delta\theta\ \theta=o}^{\theta=\mathrm{arc}\cos\frac{1}{V}} K^{*1}_{r,\theta}[1 - \frac{1}{V\cos\theta}]\exp(-\Sigma_\alpha r\cos\theta)$$

$$\sin\theta\cos\theta\Delta r\Delta\theta$$

$$+ \sum_{\Delta r\ r=L}^{r=R_c^\circ} \sum_{\Delta\theta\ \theta=\mathrm{arc}\cos\frac{L}{r}}^{\theta=\mathrm{arc}\cos\frac{1}{V}} K^{*1}_{r,\theta}[1 - \frac{1}{V\cos\theta}]\exp[-\Sigma_\alpha r\cos\theta)$$

$$\sin\theta\cos\theta\Delta r\Delta\theta \quad , \tag{3.52}$$

where

$$K^{*1}_{r,\theta} = Vr_3 \qquad \text{if } Vr_3 < R_r \quad ,$$

$$r_2 = [\frac{r}{R_c^\circ} - 1]R_r^\circ\cos\theta + r_{3m} \quad ,$$

and

$$K^{*1}_{r,\theta} = R_r \qquad \text{if } Vr_3 > R_r \quad .$$

$K^{*1}_{r,\theta}$ assumes the value zero whenever $K^{*1}_{r,\theta}$ is negative. When $L > R_c^\circ$, then the second summation is zero, and the upper limit of the first summation ($r = L$) becomes R_c°.

The total optical density for the front recorder case is therefore the sum of D_I and D_{II} (Eq. (3.52) and Eq. (3.51) respectively or

$$D_f = D_I + D_{II} \quad . \tag{3.53}$$

The optical density of the back recorder system can be obtained by simply substituting $- \Sigma_\alpha$ for Σ_α in the front recorder system and by including a normalization factor to give

$$D_b = \exp[- \Sigma_\alpha L] D_f(\Sigma_\alpha \rightarrow - \Sigma_\alpha) \quad . \tag{3.54}$$

This is basically a reversal of the incident neutron beam direction. The central converter system can now be written as the sum of the back and front recorder systems:

$$D_t = D_f + D_b \quad . \tag{3.55}$$

It should be noted, that for very small converter thicknesses ($L < 10$ μm), the upper limit of Case II is a function of the converter thickness and not a constant. This is caused by the critical angle limitations, Fig. 5. It is also assumed that all charged particles come to a stop inside the recorder so that the track etching is not force-ended due to insufficient recorder thickness.

3.4 Application of the Theory to the Lithium-6 Converter, Triton and Alpha-Particle Recording, Central Converter System

The recording film used consists of a cellulose-nitrate layer, of 8 μm thickness, supported by a 100 μm clear plastic base. The layer etched away, r_{3m}, is assumed to be 2.6 μm.[7] The range of converter thickness used is between 10 μm and 200 μm. The constants are taken from A.A. Harms, M.S. Moniz,[6] and are summarized in Table I.

First the triton contribution is considered. The converter volumes contributing to the recorded triton tracks are illustrated in Fig. 5(a),(b). The two cases shown are:

(a) The converter thickness, L, is 150 μm (the active triton contributing domains are cross-hatched).

(b) The converter thickness is 40 μm.

For these cases, the limits for the angular and radial integrations are clearly shown, Fig. 5. The calculations are done as outlined in the above theory (3.1-3.3) and it was assumed that the etching is in no case terminated by the supporting plastic film. The summation, Eq. (3.52) was done by dividing the angular (θ) and radial (r) ranges into 200 partitions, or

$$\Delta r = \frac{R_c}{200} \quad , \tag{3.56}$$

and

$$\Delta\theta \approx \frac{\pi}{400} \quad . \tag{3.57}$$

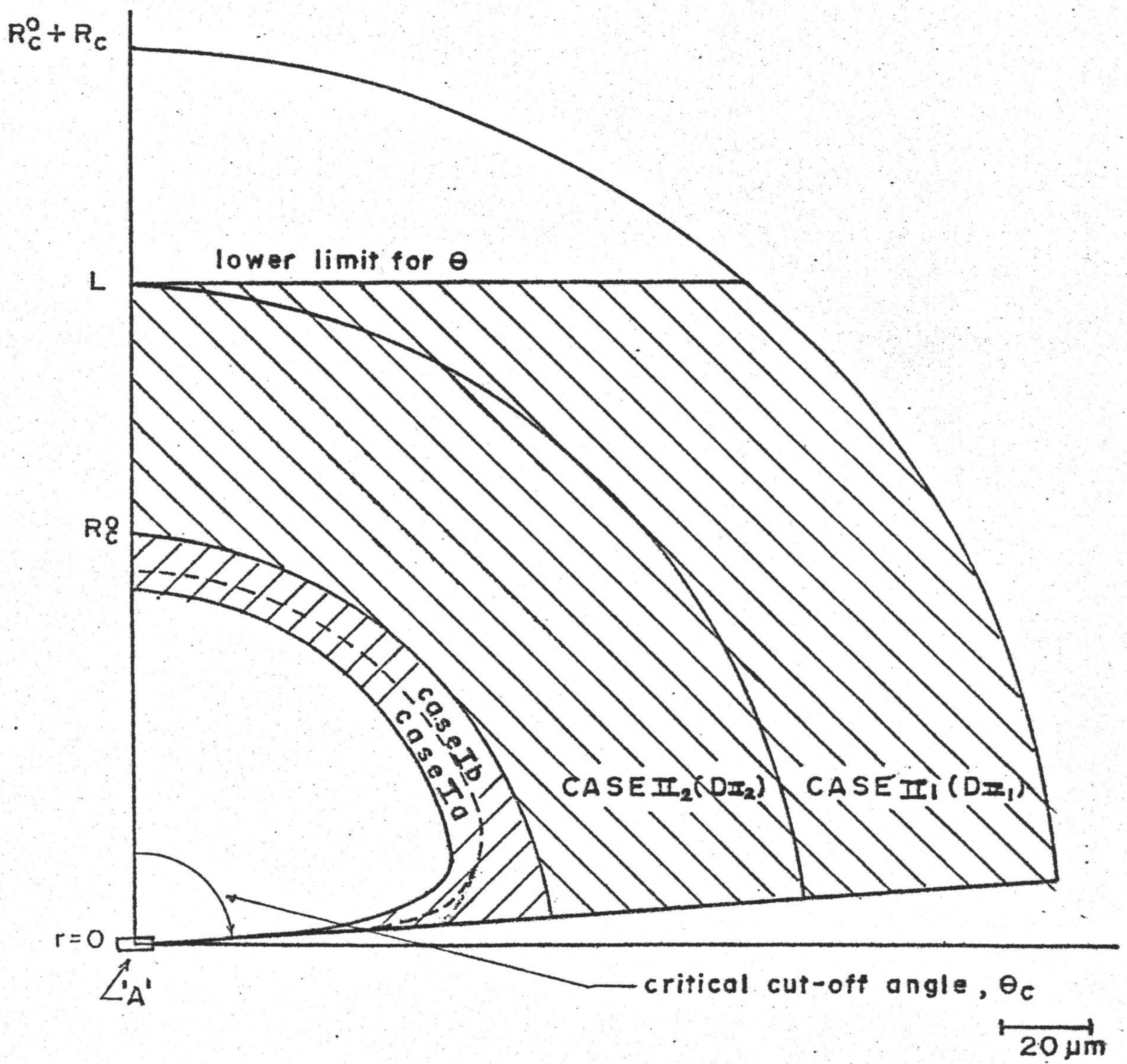

Fig. 5(a): Track etch formation domains for a converter thickness of 150 μm

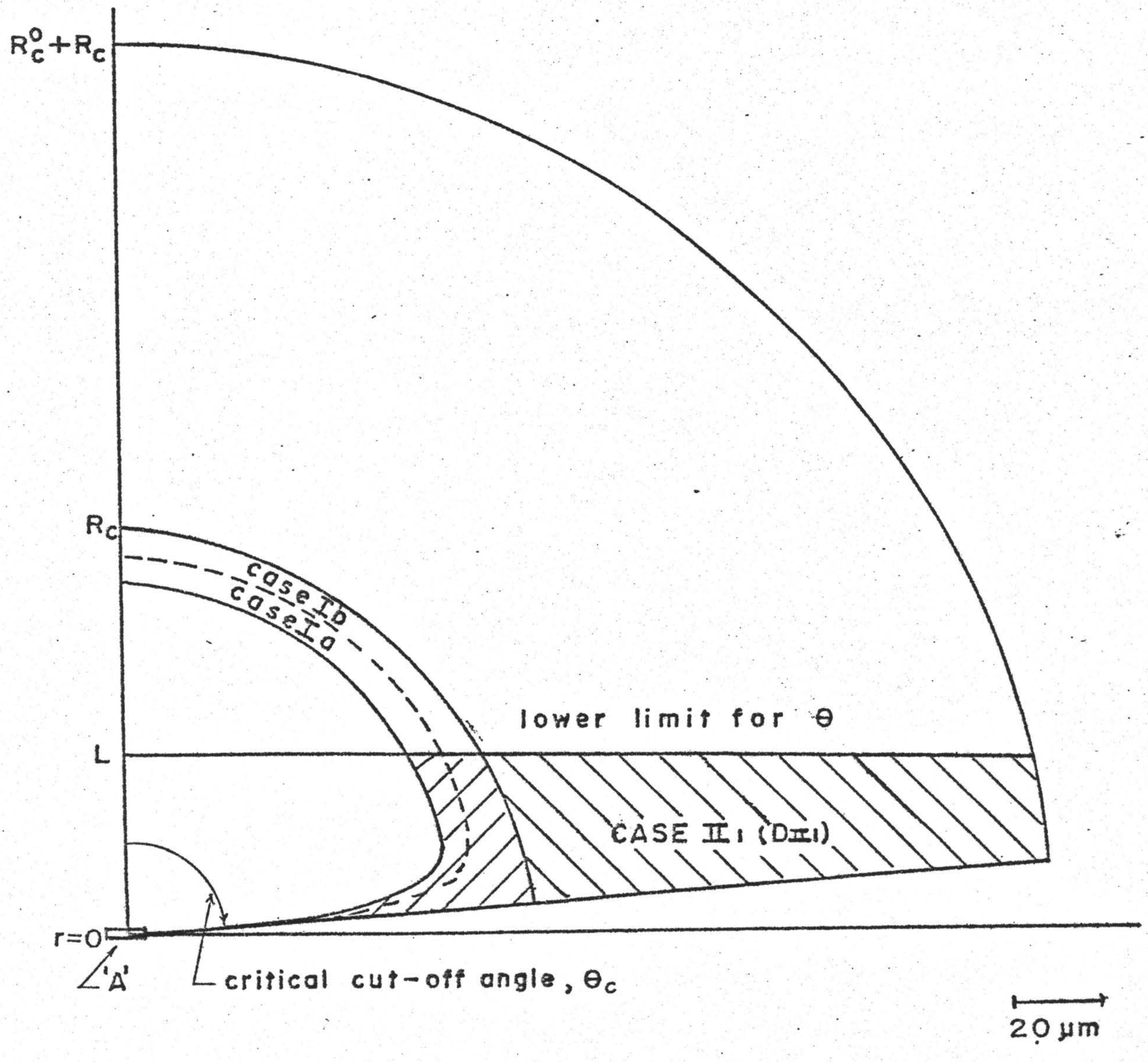

Fig. 5(b): Track etch formation domains for a converter thickness of 40 μm

Using 400 partitions changed the results by less than 2%. For Case II, it was found necessary to expand the integral solutions to third order (Power "2") for the a-terms and to the fifth order (Power "4") for the aV-terms, to produce an error of less than 2%. The required expansions are shown in Eq. (3.47) and Eq. (3.50). The results of Case I and Case II are summarized in Table II and Table III.

At this point is is necessary to calculate the α-particle density contribution. The alpha-particles are already below threshold energy,[6] and therefore, only Case II has to be considered. Since the α-particle ranges are very short (R_c = 13 μm, R_r = 3.3 μm), the previously derived theory can be considerably simplified. It can be seen that the alpha-particles contribution does not change with the converter thickness after a converter thickness of 13 μm is reached. (Except for the standard exponential attenuation in the back recorder case, (Eq. (3.54)). Only the total alpha-particle contribution is therefore of practical importance.

The optical density is given by Eq. (3.33), which, for alpha-particles, can be written as

$$D_\alpha^* = \int_{r=o}^{r=13} \int_\theta K^{*2}\left[1 - \frac{1}{V\cos\theta}\right] \exp(-\Sigma_\alpha r\cos\theta)\sin\theta\cos\theta\, d\theta\, dr \quad , \tag{3.58a}$$

where

$$K^{*2} = R_r\left[1 - \frac{r}{R_c}\right] \quad . \tag{3.58b}$$

It is noted that "exp(- $\Sigma_\alpha r\cos\theta$)" is always approximately equal to 0.98 with the actual range from 0.96 to 1.00. The exponential term is therefore considered to be constant, hence

$$D_\alpha^* = .98R_r \int_{r=u}^{r=13} (1 - \frac{r}{R_c}) \int_{\theta=o}^{\theta=\arccos\frac{1}{V}} (1 - \frac{1}{V\cos\theta})\sin\theta\cos\theta d\theta dr \quad . \tag{3.59}$$

Letting u = cosθ , and solving the angular integral, we obtain

$$D_\alpha^* = .98R_r \int_o^{13} (1 - \frac{r}{R_c})[- \int_1^{\frac{1}{V}} udu + \frac{1}{V}\int_1^{\frac{1}{V}} du]dr \quad , \tag{3.60}$$

or

$$D_\alpha^* = .98R_r[\frac{1}{2V^2} - \frac{1}{V} + \frac{1}{2}] \int_o^{13} (1 - \frac{r}{R_c})dr \quad . \tag{3.61}$$

After solving the radial integral, Eq. (3.61) can be written as

$$D_\alpha^* = .98R_r[\frac{1}{2V^2} - \frac{1}{V} + \frac{1}{2}][13 - \frac{13^2}{2R_c}] \quad , \tag{3.62}$$

where R_r, R_c, and V are given in Table I. Now a correction factor, taking the different crater diameters of alpha-particles versus tritons into account, is introduced in the form

$$\frac{\xi_\alpha}{\xi_t} = \frac{1}{.75} \quad . \tag{3.63}$$

Hence the weighted optical density is given by

$$D_\alpha = D_\alpha^* \frac{\xi_\alpha}{\xi_T} \quad , \tag{3.64}$$

or

$$D_\alpha = 12(\mu m^2) \quad . \tag{3.65}$$

Table IV gives this result in terms of different converter thicknesses for both front- and back-recorder systems. The combined results of Tables II and IV, and Tables III and IV are shown in Fig. 6 and Fig. 7 respectively. The central converter system densities are summarized in Table V and shown in Fig. 8. The previously obtained curve by A.A. Harms, M.S. Moniz,[6] for a one-dimensional model, is also given for comparison. It can be seen that by including angular density contributions, the distribution is considerably changed.

Table I: Track-etch parameters used in the analysis. This data was extracted from Ref. 1 and Ref. 6.

Parameter	Triton Range (μm)	Alpha-particle Range (μm)
R_c°	91	0
R_c	107	13
R_c°	27	0
R_r	6.7	3.3

$\Sigma_\alpha = 0.0043\ \mu m^{-1}$

$V = 14$

Table II: Comparison between the integral of Case I front and back recorder triton optical density, as a function of the lithium converter thickness as obtained from theory.

Lithium thickness (μm)	Front recorder density (arbitrary units)	Back recorder density (arbitrary units)
10	1.4	1.4
20	4.9	5.0
30	9.0	9.2
50	17.4	18.0
75	27.5	28.8
91	32.2	33.2
100	32.2	31.9
150	32.2	25.8
180	32.2	23.0
200	32.2	20.8

Table III: Comparison between the integral of Case II front and back recorder triton optical densities, as a function of the lithium converter thickness as obtained from theory.

Lithium thickness (μm)	Front recorder density (arbitrary units)	Back recorder density (arbitrary units)
10	2.0	2.0
20	4.0	4.0
30	7.0	7.0
50	20.0	21.0
75	46.0	51.0
91	67.0	76.0
100	76.0	90.0
150	105.0	113.0
180	108.0	104.0
200	109.0	96.0

Table IV: Comparison between the integral of Case II front and back recorder alpha-particle optical densities, as a function of the lithium converter thickness as obtained by theory.

Lithium thickness (μm)	Front recorder density (arbitrary units)	Back recorder density (arbitrary units)
13	12	12
20	12	11
30	12	11
50	12	10
75	12	9
91	12	8
100	12	7
150	12	6
180	12	6
200	12	5

Table V: Alpha-particle and triton total optical density contributions, for front-, back-, and central converter systems as a function of the lithium converter thickness.

Lithium thickness (μm)	Front recorder density (arbitrary units)	Back recorder density (arbitrary units)	Central converter density (arbitrary units)
10	13	13	27
20	21	20	41
30	28	27	55
50	49	49	98
75	86	89	174
91	111	117	228
100	120	129	249
150	149	145	294
180	152	133	285
200	153	122	275

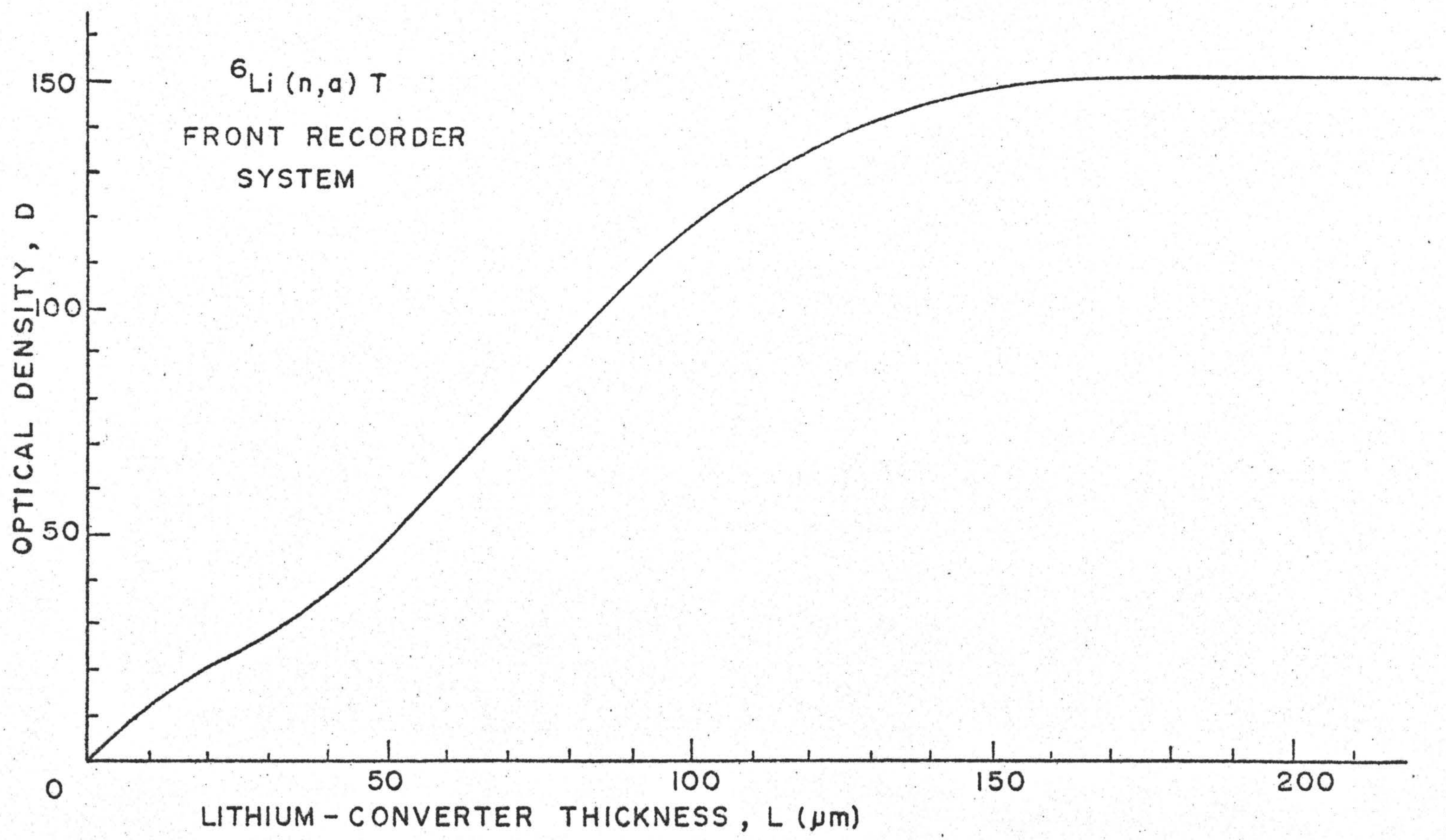

Fig. 6: Dependence of optical density on Lithium-6 converter thickness for the front recorder system

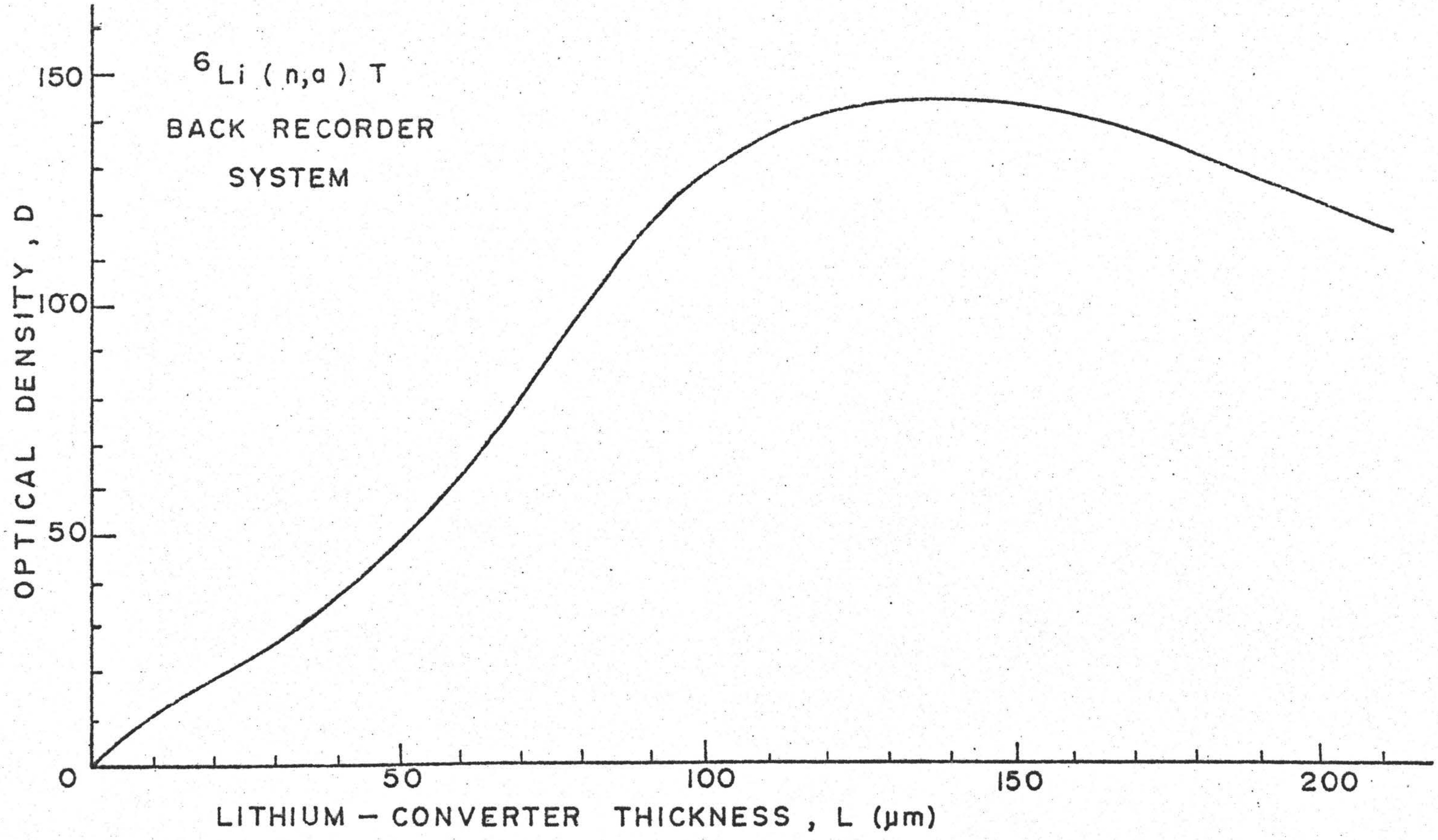

Fig. 7: Dependence of optical density on Lithium-6 converter thickness for the back recorder system

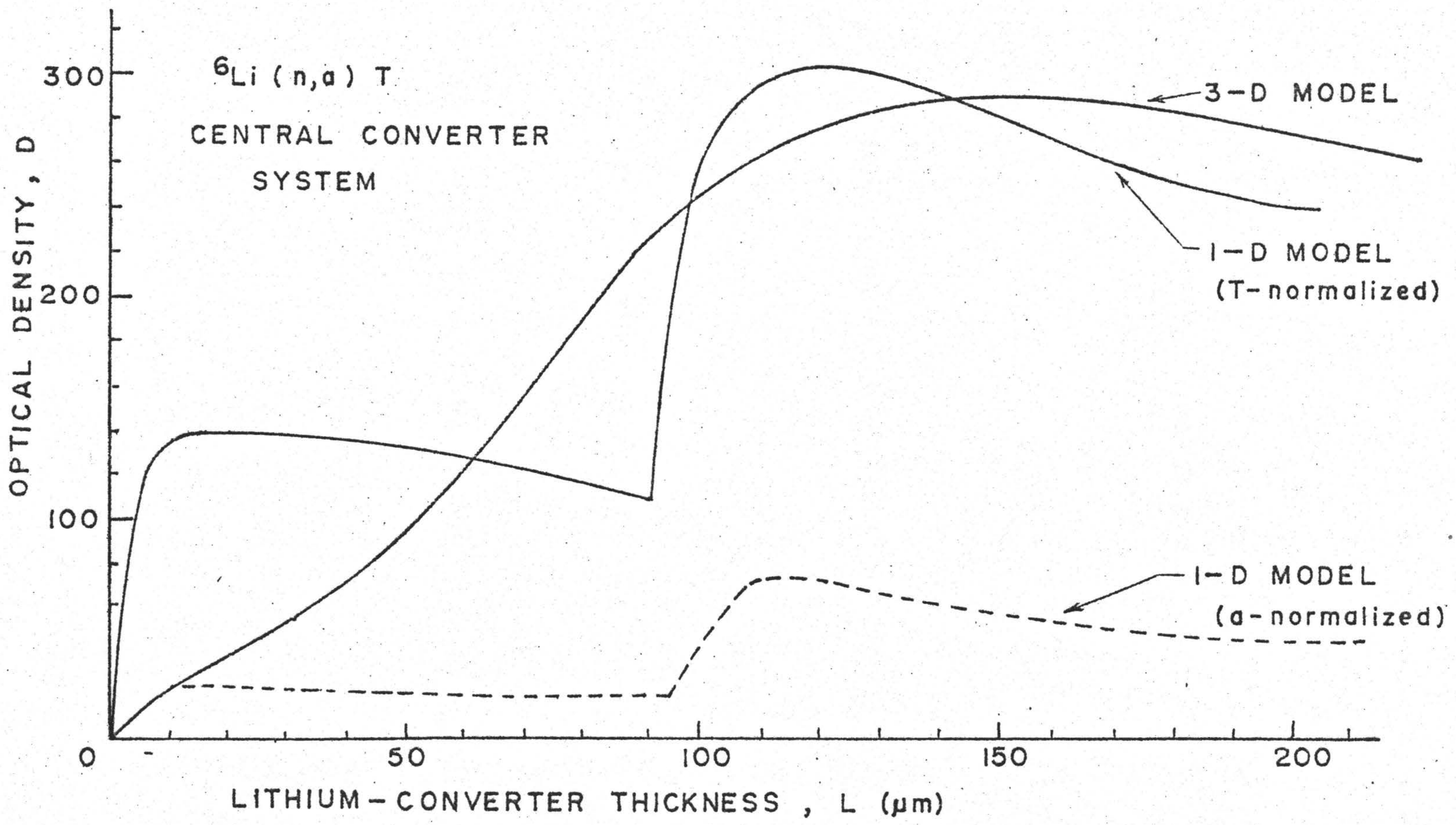

Fig. 8: Comparison between the one-dimensional optical density model and the three-dimensional optical density model for the central converter system

CHAPTER 4

EXPERIMENTAL DATA ANALYSIS AND RESULTS

4.1 Method Descriptions

The track etch films were analyzed by the following methods.

Method I: Visual data from micrographs (magnification 1000X) obtained from:

(a) electron micrographs, and

(b) photon micrographs.

This method was used for track counting and track investigations for track-size and shape and film transmission-reflection information.

Method II: Measured data of transmitted light using a spot densitometer by using

(a) "white" light,

(b) green light (5600 Å), and

(c) red light (6600 Å filter).

From this data, the optical density is obtained by the definition:[10]

$$\text{optical density (D)} = \log_{10} \frac{1}{\text{Transmission}} \tag{4.1}$$

(all optical transmission data are normalized to 100% at points where no conversion occurred).

Before actual data are presented, these methods are discussed and then only relevant data will be given.

4.2 Discussion of the Measurement Techniques

Through Method I, valuable information concerning the optical density of the films could be obtained. It was needed for both the design of the theoretical model and the interpretation of the data obtained by Method II. Counting tracks proved to be a very unreliable method of density determinations. Due to the focussing of the microscope (transmission), different hole populations were brought into focus with different settings. The hole count was therefore influenced by the depth of the focal plane in the cellulose-nitrate layer. The use of the human eye to judge the depth of holes under these conditions can produce results with large errors. The counting results are therefore not given.

Through Method II, reproducible optical density data was obtained. It was however, contrary to popular speculations, discovered that the highest optical densities were not obtained with the green filter but with the red filter. Since this study emphazises high contrast conditions, only the densities using the red filter are presented. Some data on the other methods will appear in the following discussions as they are needed.

4.3 Presentation of the Data

The experimental data consists of two sets of films:

(I) The Roman numeral set, and

(II) The Arabic numeral set..

Both sets are defined by Table VI.

Typical results obtained by Method I are reproduced in Fig. 9a, 9b, 9c, Fig. 10, and Fig. 11, where ΔT is defined to be the exposure time.

The red light (6600 Å) transmission data is summarized in Fig. 12 and Fig. 13 for the Roman numeral set and Arabic numeral set respectively. The aparture of the digital spot-densitometer used for these measurements had the dimensions 1.4 mm by 4.0 mm.

Table VI: The organization of the experimental data.

Type Code	Etch date	Exposure times, Δt (sec)	Lithium thickness, L (inches)
FIII BIII	10/4/75	10240	.00125,.002,.003, .004, .005
FII BII	10/4/75	5120	"
FI BI	10/4/75	2560	"
F7 B7	30/11/75	10240	.002, .003, .004, .006, .008
F6 B6	30/11/75	5120	"
F5 B5	30/1/75	2560	"
F4 B4	30/1/75	1280	"
F3 B3	30/1/75	640	"

Where F denotes the front recorder contribution of the central converter system and B denotes the back recorder contribution. The Roman numeral set also differs from the Arabic numeral set in etching procedure.

a) Set FII:

$x = 1000$,

$\Delta T = 5120$ sec,

$L = 31$ μm.

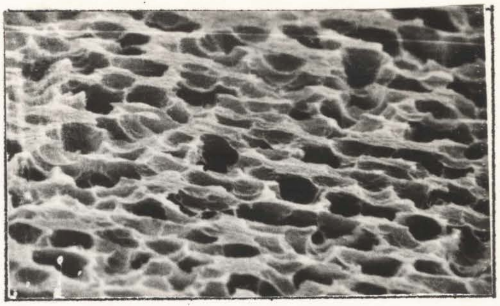

b) Set FI:

$x = 1000$,

$\Delta T = 2560$ sec,

$L = 139$ μm.

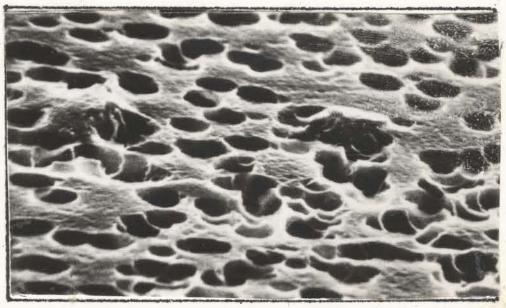

c) Set BI:

$x = 1000$,

$\Delta T = 2560$ sec,

$L = 31$ μm.

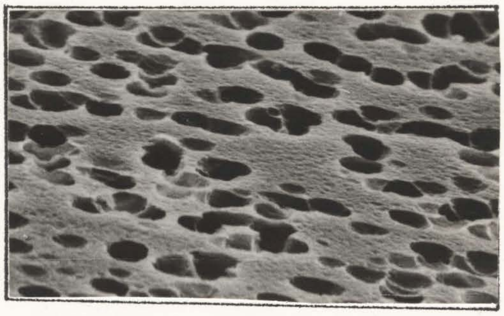

Fig. 9: Electron micrographs of etch-pit profiles at 70° of incidence

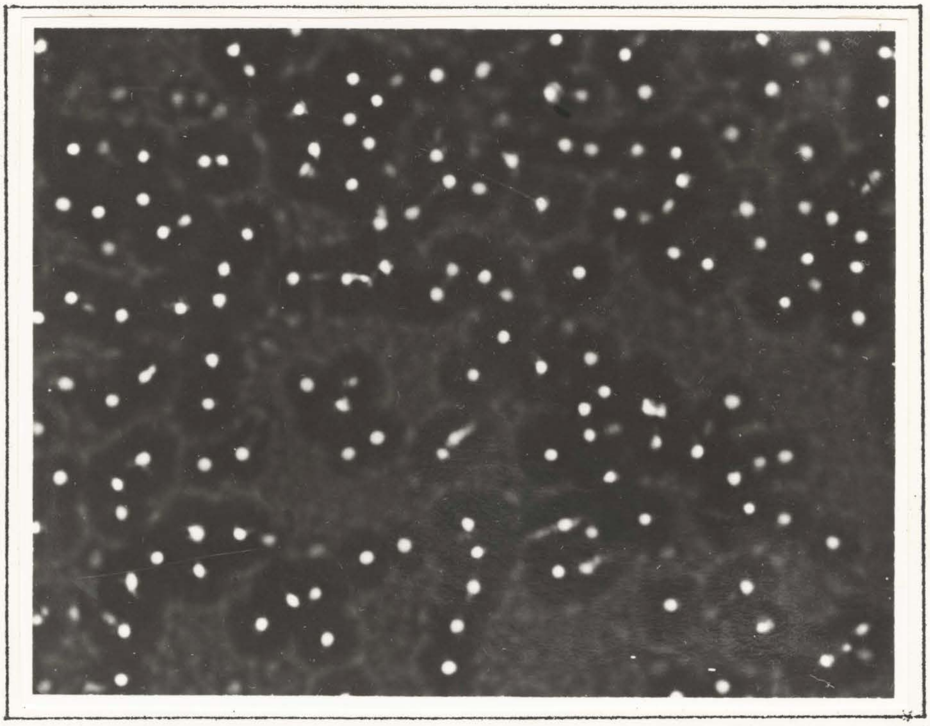

Fig. 10: Transmission photo-micrograph of CN-recorder

Set BI:

$x = 1000$,

$\Delta T = 2560$ sec,

$L = 50\ \mu m$.

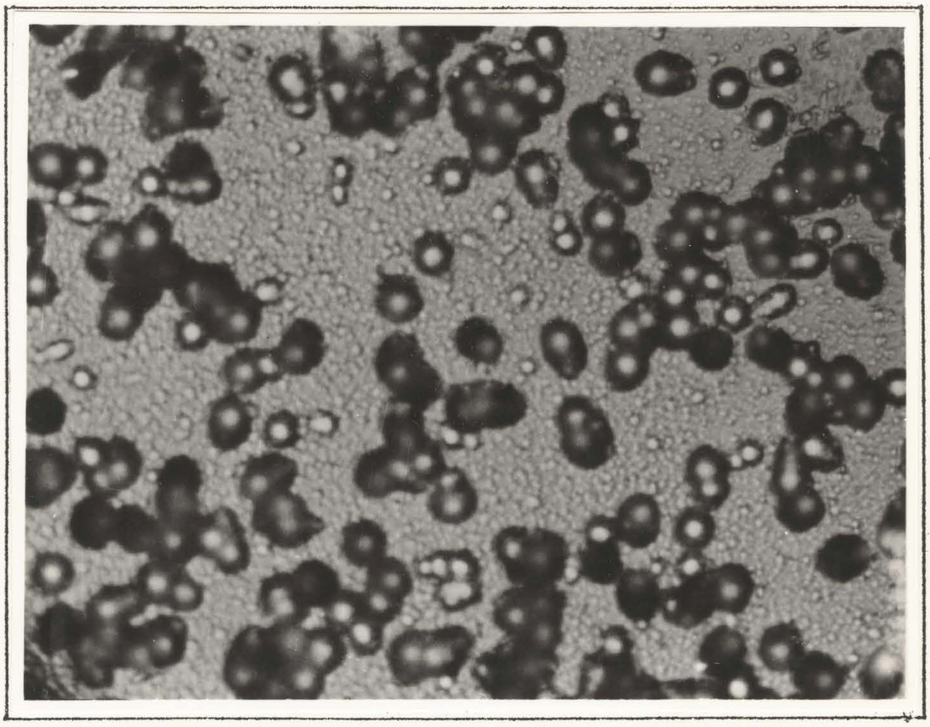

Fig. 11: Reflection photo-micrograph of CN-recorder

Set BI:

$x = 1000$,

$\Delta T = 2560$ sec,

$L = 31\ \mu m$.

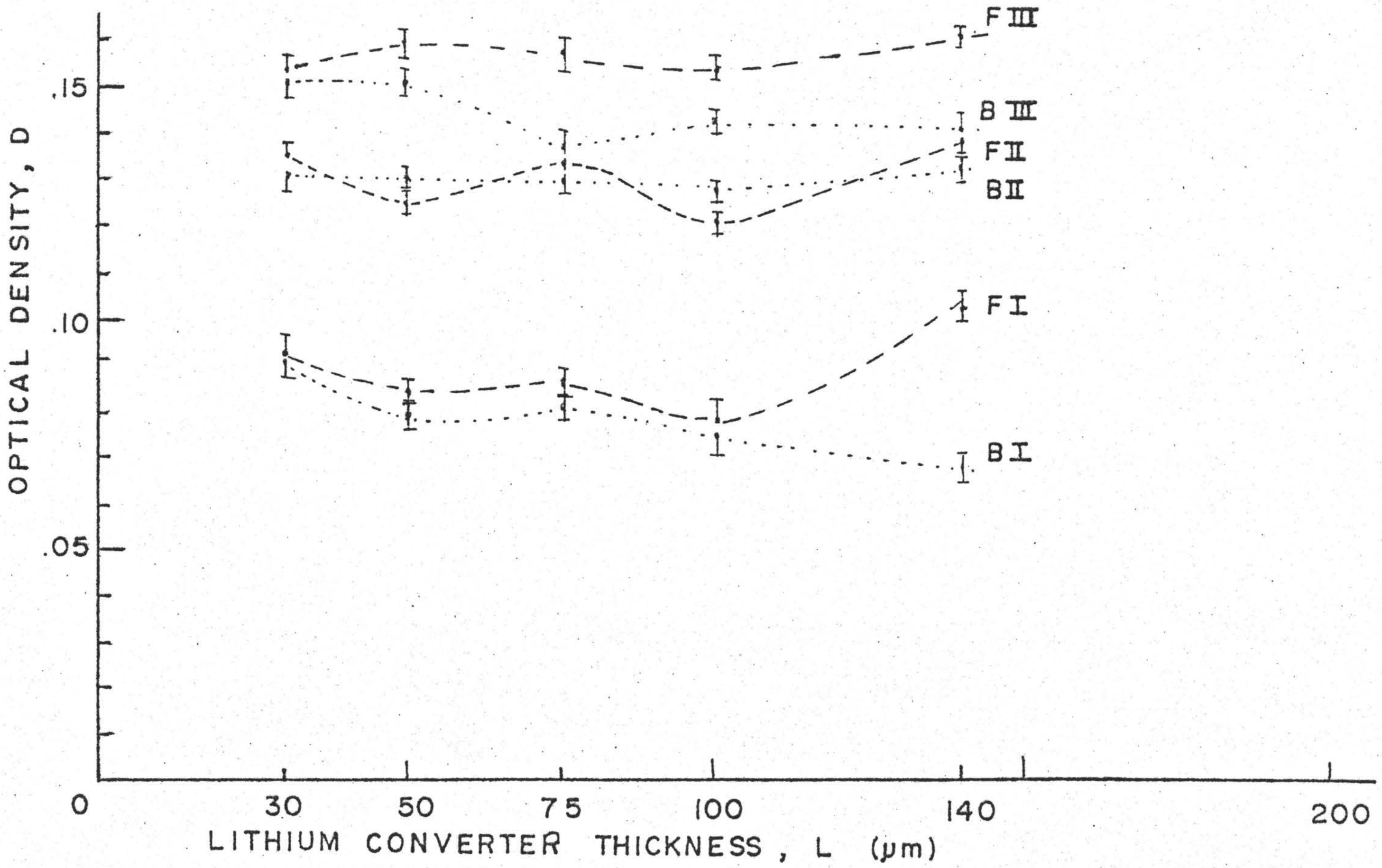

Fig. 12: Experimental transmission data of optical density versus Lithium-6 converter thickness for the Roman numeral set, obtained by using red (6600 Å) light

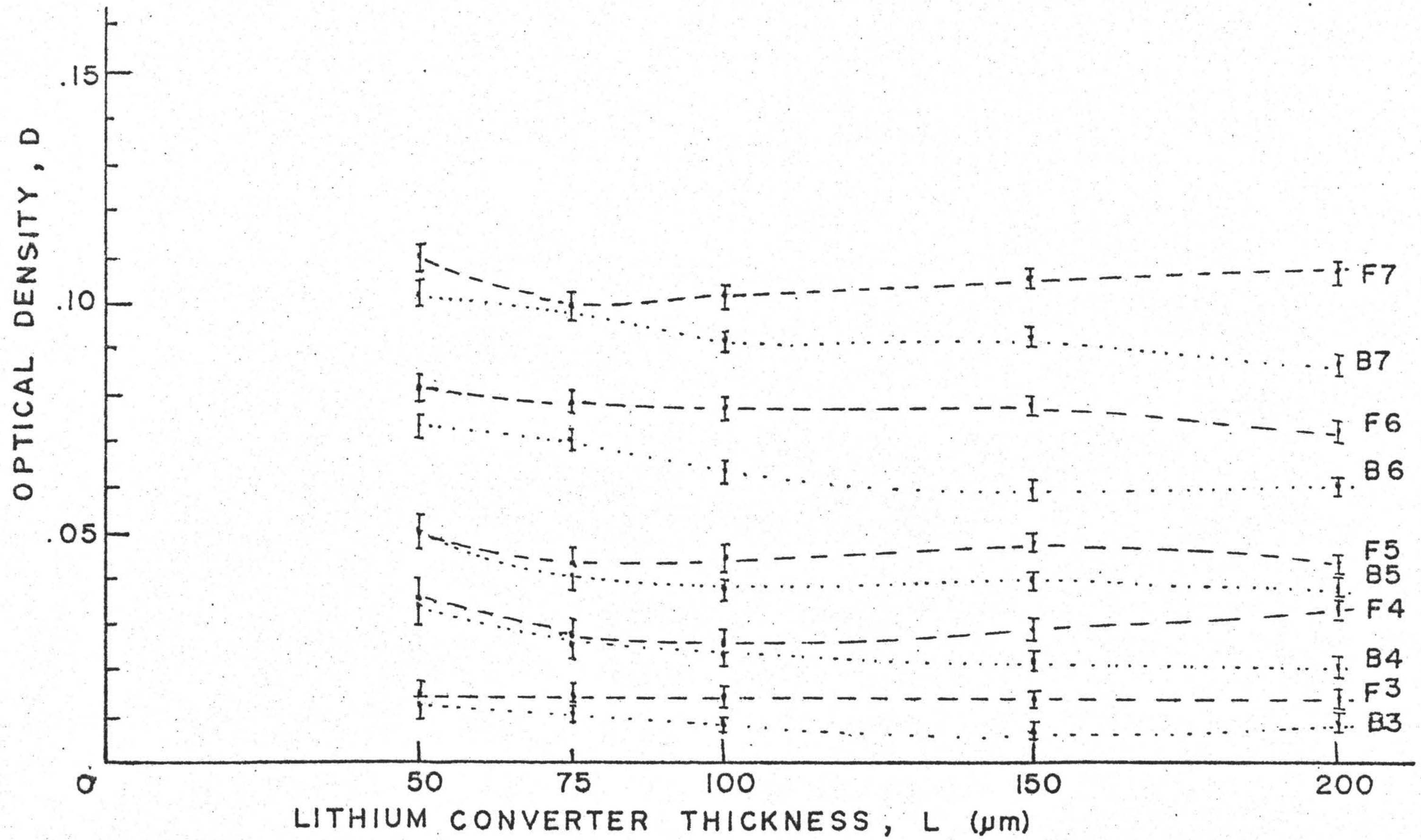

Fig. 13: Experimental transmission data of optical density versus Lithium-6 converter thickness for the Arabic numeral set, obtained by using red (6600 Å) light

CHAPTER 5

DISCUSSION OF THE RESULTS

5.1 Theoretical-Experimental Curve Fitting

By comparing Fig. 6,7, and 8 (theoretical) with Fig. 12 and 13 (experimental) it is clear that any curve-fitting cannot be done at this stage since the experimental distribution curve differs too much in shape from both theoretical curves, Fig. 8. Therefore only a non-numerical analysis, aiming to bring experimental conditions closer to the theoretical case is possible. Only after these corrections, can a curve-parameter fitting be attempted.

The basic difference between the experimental density distribution and the theoretical density distribution is that the experimental curves usually have zero slope or negative slope while the theoretical curve has a positive slope for the larger part of its range. To remedy this situation, the following problems have to be considered:

(1) cellulose-nitrate film colouration,

(2) saturation effects, and

(3) cellulose-nitrate film thickness.

5.2 Cellulose-Nitrate Film Colouration

Previously it was speculated, that holes are created by etching, the use of a transparent red film and the viewing under green light would yield the highest contrast. This however, is not true. The "F7" set, Table VI, produced average densities of 0.01 using green light, 0.08 using white light, and 0.11 using red light. Clearly the red filter (6600 Å) produces the highest density and therefore the highest contrast. To clarify this contradiction, photon and electron micrographs were made of the exposed films. Typical results are shown in Fig. 9, 10, and 11. After careful investigations of those and other micrographs, it was concluded that the walls of the etch-pits are very rugged and thus form good scatterers. Viewing the recordings under a transmission microscope, (Fig. 10), it is noted that a small area of high transmission, with a diameter of about 1 μm, which is interpreted as the flat bottom of the pit, is surrounded by a dark, circular area, with a diameter of about 7 μm which is interpreted as the steep, rugged pit wall. This dark area, due to light scattering, is the major density producing effect.

Even when a red filter is used, the effect of "hole lightening", as opposed to "scatter darkening", becomes of considerable importance only when particle tracks with an angle of incidence around $\theta = 0°$ are considered. For particle tracks that reach a considerable depth in the recorder, quite common under these conditions, the hole lightening actually seems to slightly reverse the scatter darkening. This explains why an actual dip in optical density is obtained between converter thicknesses of 75 μm and 140 μm, Fig. 12 and Fig. 13. In an attempt to find the loss in density produced by hole lightening the following estimations were made. The colouration of the film containing no etch pits produces an optical density of .06 (a .03 density correction due to reflection losses is included) under red (6000 Å) light. Using the microphotograph of "BI (30 μm)", Table VI, it was found that about 20% of the total film volume was crater volume. Therefore, a density loss between .01 and .02 can be expected. The measured density was 0.09, Fig. 12. Using a colourless film, a measured density of 0.11 can be expected. A clear colourless film would therefore increase the optical density and eliminate an early flattening of the density versus converter thickness curve. Experimental results will therefore come closer to the theoretical results as shown in Fig. 6, 7, and 8.

5.3 Saturation Effects

Saturation effects, like hole lightening, also produces an early flattening of the transmission density distributions. Overlapping etch-craters are not covered by the theory and therefore no curve fitting is possible in this region. Fig. 9a clearly shows that the Roman numeral set II, Table VI, is in the saturation region. Even Roman numeral set I shows some pit-overlapping, as can be seen in Fig. 9b, 9c, and Fig. 11. Fig. 10 shows the same effect but care has to be exercised not to confuse the actual pit border with the border of the low density, flat pit bottom. This error was made previously and produced the conclusion that Roman numeral sets II and III were not in the saturation region. The transmission densities given by Fig. 12 also show that sets II and III are in the saturation region. The same applies for the Arabic numeral set. For this set, etch conditions were slightly different and it appears that the sets 3, 4, 5, and possibly 6 are all in the linear density region, Fig. 13.

In conclusion, it can be mentioned that saturation effects are not only undesirable for theoretical-experimental curve fitting but also the optical density versus exposure time efficiency is reduced.

5.4 Cellulose-Nitrate Film Thickness

Since an 8 μm thick cellulose nitrate layer is used and the maximum depth of an etch-pit is about 6.7 μm, forced termination of the crater etching due to the supporting clear plastic should be negligible. In fact, microphotographs show that only about 3% of the craters penetrate the active film layer completely. Errors similar to "hole lightening" can occur since forced etch termination produces extra-large flat pit bottoms thus increasing the transmission of the film and reducing the density. To avoid any complications, the cellulose nitrate film thickness should be increased to at least 10 μm. (A word of caution should be added here. Fig. 10 cannot be used to determine which pits penetrate the active layer completely. In this reproduction, taken from a colour microphotography, the background and the scatter darkened regions were moved into the linear region of the D-H curve.[10] The relatively bright pit bottoms are therefore due to overexposure. To find the number of completely penetrating etch tracks, considerable care has to be exercised so that the bright pit bottoms are both in focus and in the linear region of the D-H curve.)

CHAPTER 6

CONCLUSIONS

It can be concluded that to maximize contrast, a clear and colourless cellulose nitrate film, approximately 150 μm thick, such as Kodak-Pathe Type Ca-8015, should be used. Eastman Kodak Type 106-01, possessing a 8 μm clear cellulose nitrate layer on a 100 μm thick inactive polyester base, can also be used but etch conditions have to be carefully controlled so as not to "over-etch" the film. Lithium converter thicknesses should be between 25 μm and 200 μm, and exposure times should be between 640 sec and 10240 sec.

From theoretical considerations, it can be concluded that the alpha-particle contribution is 8% of the total alpha-particle and triton contribution taken at a lithium thickness of 140 μm. A converter thickness of 140 μm gave the maximum optical density or contrast when a central-converter system is used. The recorded alpha-particles and tritons could not be distinguished from each other, since the particles have overlapping energy ranges.

REFERENCES

1. R.L. Fleischer, P.B. Price, and R.M. Walker, "Track Registration in Various Solid-State Nuclear Track Detectors", Physical Review, 133, A1443 (1964).
2. R.L. Fleischer, H.W. Alter, S.C. Furman, P.B. Price, and R.M. Walker, "Particle Track Etching", Science, 178, 255 (1972).
3. R.L. Fleischer, P.B. Price, R.M. Walker, "Tracks of Charged Particles in Solids", Science, 149, 383 (1965).
4. R.H. Stinson, "Boron Autoradiography of Botanical specimens", Canadian Journal of Botany, 50, 245 (1972).
5. H. Berger, "Track-Etch Radiography: Alpha, Proton, and Neutron", Nuclear Technology, 19, 188 (1973).
6. A.A. Harms and M.S. Moniz,,"Track-Etch Imaging Efficiencies of the $^{10}B(n,\alpha)^{7}Li$ and $^{6}Li(n,\alpha)T$ Reactions", Nuclear Instruments and Methods, 122, 567 (1974).
7. R.H. Stinson, P.A. Egelstaff, and T.M. Holden, "A High Resolution Neutron Camera for Diffraction Experiments", Canadian Journal of Physics, 53, 52 (1975).
8. M.S. Moniz, "An Investigation of Image Formation in Track-Etch Radiography", unpublished B.Eng. Thesis (1974).
9. Standard Mathematical Tables, The Chemical Rubber Co.
10. R.H. Herz, The Photographic Action of Ionizing Radiations, Wiley Interscience, New York, 1969.

11. V.E. Pilcher, C.C. Jones, and G.R. Ellmers, "Particle Tracks in Cellulose-Nitrate", American Journal of Physics, 40, 679 (1972).